Performance Evaluation of ANCF Tetrahedral Elements in the Analysis of Liquid Sloshing

Dayu Zhang
School of Astronautics,
Northwestern Polytechnical University,
Xi'an, Shaanxi 710072, China
e-mail: dyzhang@mail.nwpu.edu.cn

Emanuele Grossi
Exponent,
525 West Monroe Street,
Suite 1050,
Chicago, IL 60661
e-mail: egrossi@exponent.com

Ahmed A. Shabana[1]
Department of Mechanical and Industrial Engineering,
University of Illinois at Chicago,
842 West Taylor Street,
Chicago, IL 60607
e-mail: shabana@uic.edu

The performance of the absolute nodal coordinate formulation (ANCF) tetrahedral element in the analysis of liquid sloshing is evaluated in this paper using a total Lagrangian nonincremental solution procedure. In this verification study, the results obtained using the ANCF tetrahedral element are compared with the results of the ANCF solid element which has been previously subjected to numerical verification and experimental validation. The tetrahedral-element model, which allows for arbitrarily large displacements including rotations, can be systematically integrated with computational multibody system (MBS) algorithms that allow for developing complex sloshing/vehicle models. The new fluid formulation allows for systematically increasing the degree of continuity in order to obtain higher degree of smoothness at the element interface, eliminate dependent variables, and reduce the model dimensionality. The effect of the fluid/container interaction is examined using a penalty contact approach. Simple benchmark problems and complex railroad vehicle sloshing scenarios are used to examine the performance of the ANCF tetrahedral element in solving liquid sloshing problems. The simulation results show that, unlike the ANCF solid element, the ANCF tetrahedral element model exhibits nonsmoothness of the free surface. This difference is attributed to the gradient discontinuity at the tetrahedral-element interface, use of different meshing rules for the solid- and tetrahedral-elements, and the interaction between elements. It is shown that applying curvature-continuity conditions leads, in general, to higher degree of smoothness. Nonetheless, a higher degree of continuity does not improve the solution accuracy when using the ANCF tetrahedral elements. [DOI: 10.1115/1.4048464]

Keywords: tetrahedral element verification, liquid sloshing, absolute nodal coordinate formulation, curvature continuity

1 Introduction

The main objective of this verification study is to evaluate the performance of the absolute nodal coordinate formulation (ANCF) tetrahedral element in the analysis of liquid sloshing. To this end, the results obtained using the ANCF tetrahedral element are compared with the results obtained using the ANCF solid element, which has been previously subjected to numerical verification and experimental validation in liquid sloshing applications. Liquid-sloshing effect cannot be ignored in many engineering applications, including highway and rail transportation, marine, and aerospace systems [1–3]. Accurate evaluation of the sloshing effect is necessary in order to avoid deadly, environmentally damaging, and costly accidents; and in order to be able to develop credible operation and safety guidelines for transportation systems. Virtual prototyping for the evaluation of sloshing scenarios must be based on approaches that realistically represent the fluid dynamics. The motion of the fluid is governed by the Navier–Stokes equations which are expressed in terms of the time-rate of the position gradients. Finite element (FE) models that do not ensure the continuity or a certain degree of smoothness of the position gradients at the FE interfaces can lead to jump discontinuities in the viscosity forces even in the cases of laminar flow.

In the computer implementation, the viscosity forces are evaluated at the integration points, some of which are not nodal points and are located at the interface surfaces. A cubic Bezier surface can be defined in terms of three polynomials, each of which represents a coordinate along one of three orthogonal axes. Each of the polynomials representing a Bezier surface has 16 coefficients, making the total number of coefficients required to represent the three-dimensional surface 48 coefficients. A surface of an ANCF solid element has four nodes, each of which has 12 coordinates; three position coordinates and three gradient vectors. Therefore, imposing continuity on the position and position gradients at the nodal points of two neighboring elements, ensures that the interface surfaces between the two elements are identical, and consequently, there are no gaps or gradient discontinuities at the element interface surfaces. This is, however, not the case when ANCF tetrahedral elements are used because interface surfaces can have only three nodal points leading to 36 conditions which are not sufficient to ensure that the two surfaces of the two neighboring elements at the interface are identical. Because tetrahedral elements can be used to capture geometric details more conveniently, this paper addresses this fundamental geometry problem in liquid sloshing and examines the use of curvature continuity constraints in order to achieve a higher degree of smoothness at the tetrahedral element interfaces.

2 Approaches and Scope of this Investigation

In liquid sloshing problems, the effect of the inertia forces can be significant because of the large displacements of the containers, particularly in the case of transportation systems. The effect of turbulence, on the other hand, may be neglected because the focus is on the effect of the nominal fluid motion on the vehicle dynamics and stability. Therefore, in sloshing problems, regardless of whether or not turbulence occurs, both the inertia and viscosity forces must be taken into consideration. The development of analytical liquid-sloshing approaches is challenging because of the high dimensionality of the problem and strong nonlinearity of the fluid boundary conditions. Simple fluid models are often used to describe the fluid dynamics. Previous contributions in this area were focused on developing simple discrete inertia fluid models;

[1]Corresponding author.

Manuscript received January 30, 2020; final manuscript received August 6, 2020; published online October 15, 2020. Assoc. Editor: Amit Shukla.

in some of which the fluid is represented by rigid pendulums or mass-spring-dashpot systems [4–9]. However, these models do not capture the effect of the fluid distributed inertia and viscosity, nor the shape of the free surface [10].

Most of the numerical methods developed to solve liquid sloshing problems are based on two different approaches, Lagrangian and Eulerian [11–15]. The Lagrangian approach traces the fluid material points to define the location of the fluid free surface. The main shortcoming of this approach is the loss in numerical accuracy resulting from the large fluid displacements, and consequently, use of automatic remeshing may be necessary. On the other hand, the Eulerian approach, which focuses on the fluid movement inside a control volume, requires additional efforts to capture the fluid free surface. Furthermore, the Eulerian approach does not allow for straight forward integration of sloshing models with multibody system (MBS) algorithms which are based on a Lagrangian description.

Several mesh-free methods were proposed for the study of fluid dynamics problems using the Lagrangian approach, such as the fully Lagrangian meshless *smoothed particle hydrodynamics* that can describe complex fluid motion, including turbulent and multiphase flows [16–20]. However, the high computational cost and the large number of degrees-of-freedom (DOF) required to obtain accurate solutions makes mesh-free methods impractical and inefficient for MBS implementations. In order to address this concern, Wang et al. [21] proposed a lower order model based on the *floating frame of reference* (FFR) formulation. While such a continuum-based approach can capture the free surface of the fluid and results in a significant computational cost reduction, it cannot describe very large fluid displacements due to the use of linear modes.

Arbitrary Lagrangian-Eulerian (ALE) methods have been proposed in order to combine the advantages of the Lagrangian and Eulerian schemes. In the ALE formulations, the motions of the mesh and the material points are both described, therefore, the convective term in the momentum and continuity equations is not negligible. ALE methods are widely used in the solution of viscous, free-surface fluid problems [22–27].

Co-simulations have also been used for the integration of fluid and MBS algorithms. Using this approach, two or more software run at the same time and exchange information at predefined time steps. However, the main challenge of the cosimulation approach is the difficulty of establishing efficient communications between different algorithms and software that are based on fundamentally different approaches. Furthermore, use of cosimulations can lead to a high computational cost as the result of using large number of degrees-of-freedom.

The total Lagrangian fluid approach allows for a systematic integration with detailed vehicle models developed using MBS algorithms. Wei et al. [28] developed a total Lagrangian nonincremental liquid sloshing model based on the FE *absolute nodal coordinate formulation* (ANCF). This solution procedure was verified by Grossi and Shabana [29], and used to evaluate the effect of breaking waves in liquid sloshing problems [30]. This approach was integrated with a railroad vehicle model and a tanker truck model, respectively, [31,32]. The ANCF approach was used to study the effect of crude oil sloshing on railroad vehicle systems [33]. In the previously published work, the liquid was meshed using ANCF solid elements.

The main goal of this paper is to perform a numerical verification study to evaluate the performance of the ANCF tetrahedral finite element in solving liquid sloshing problems. The liquid container can assume large displacements including rotations. Several examples, including liquid/ground interaction, liquid sloshing in a rectangular container, and a railroad tank are considered. This paper makes the following specific contributions:

(1) To numerically verify the tetrahedral-element results, a new total Lagrangian fluid model, developed using ANCF tetrahedral elements, is integrated with computational MBS algorithms to allow for developing detailed sloshing/vehicle models.
(2) The paper presents an analytical and numerical comparative study of the performance of the ANCF tetrahedral and solid elements in the analysis of liquid sloshing problems. The liquid-sloshing results of the ANCF solid elements have been previously verified and validated.
(3) While tetrahedral elements are recommended in the case of complex geometries, the paper identifies subtle tetrahedral-geometry problems that have not been fully examined in the literature, particularly when using ANCF elements.
(4) The discontinuity problem at the ANCF tetrahedral-element interface is examined and general *curvature-continuity* conditions are used to achieve a higher degree of smoothness.
(5) Based on the verification study conducted in this paper, the limitations of the ANCF tetrahedral element in the analysis of liquid sloshing are identified in order to define the range of applicability of such elements in future investigations.

This paper is organized as follows. In Sec. 3, the fluid constitutive model is described and the ANCF displacement field of the tetrahedral element is defined. Section 4 introduces the *curvature-continuity* conditions used in this investigation to obtain a higher degree of smoothness. Sections 5 and 6 present, respectively, the MBS governing equations of motion and the fluid contact model used in this study. Section 7 presents the numerical results of two sloshing benchmark problems and a complex railroad sloshing/vehicle example. This section also discusses the limitations of the ANCF tetrahedral elements as compared to the ANCF solid element and explains the discontinuity problem at the tetrahedral element interface. Section 8 presents summary and main conclusions drawn from this investigation.

3 Basic Fluid, Geometry, and Finite Element Equations

A summary of the equations governing the fluid motion and ANCF fluid geometry used in this study is presented in this section. The displacement field of the ANCF tetrahedral element used in this investigation is also defined in this section.

3.1 Continuum Mechanics and Geometry. The fluid continuity equation can be written in the form $\partial\rho(\mathbf{r},t)/\partial t + \nabla\cdot(\rho\mathbf{v}) = 0$, where ρ is the mass density, t is time, $\mathbf{r}$ and $\mathbf{v}$ are the position and velocity vectors, respectively. For incompressible fluids, the continuity equation reduces to $\nabla\cdot\mathbf{v} = 0$. The fluid partial differential equation of equilibrium can be written as $(\nabla\cdot\boldsymbol{\sigma})^T + \mathbf{f}_b - \rho\mathbf{a} = \mathbf{0}$, where $\boldsymbol{\sigma}$ is the Cauchy stress tensor, $\mathbf{f}_b$ is the vector of body forces, and $\mathbf{a}$ is the acceleration vector, defined as $\mathbf{a} = \partial\mathbf{v}(\mathbf{r},t)/\partial t + \mathbf{v}\cdot\nabla\mathbf{v}$ [34]. The constitutive equation for a Newtonian isotropic fluid is

$$\boldsymbol{\sigma} = [-p + \lambda\mathrm{tr}(\mathbf{D})]\mathbf{I} + 2\mu\mathbf{D} \tag{1}$$

where p is the hydrostatic pressure, μ is the coefficient of dynamic viscosity, $\lambda + (2\mu/3)$ is the coefficient of bulk viscosity, tr is the trace of the matrix, and $\mathbf{D}$ is the rate of deformation tensor. If $\lambda + (2\mu/3) = 0$, one has Stokes' relation. Substituting Eq. (1) into the equilibrium equation, the incompressible Navier–Stokes formulation is obtained as

$$\left.\begin{aligned}\mathbf{f}_b + \{-\nabla\cdot(p\mathbf{I}) + \lambda\nabla\cdot(\mathrm{tr}(\mathbf{D})\mathbf{I}) + 2\mu\nabla\cdot\mathbf{D}\}^T = \rho\mathbf{a}\\ \nabla\cdot\mathbf{v} = 0\end{aligned}\right\} \tag{2}$$

In the most general case, the fluid geometry and kinematics can be described using three different configurations, namely, the *straight*, *reference*, and *current configurations*. Let V, V_o and v be the volumes in the straight, curved-reference, and current deformed configurations, respectively, and $\mathbf{x}$, $\mathbf{X}$, and $\mathbf{r}$ be the

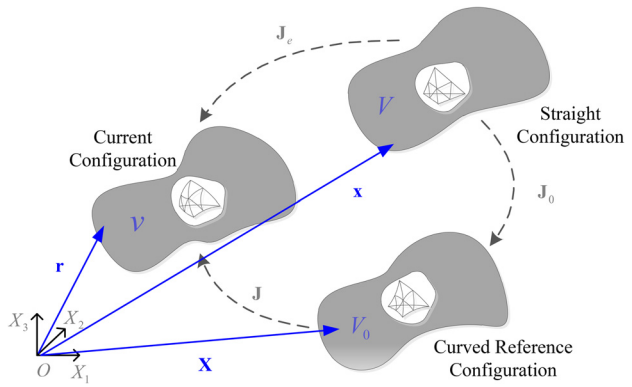

Fig. 1 The three general fluid configurations

associated position vectors in these three configurations, as shown in Fig. 1. For an ANCF element, the relation between the volumes in the reference and current configuration can be defined as $dv = JdV_o$, where $J = |\mathbf{J}|$ is the determinant of the matrix of position-vector gradients $\mathbf{J} = \partial\mathbf{r}/\partial\mathbf{X}$. Because the reference configuration can be curved, integration can be more conveniently performed by introducing the straight configuration. The relation between the volumes in the straight and reference configurations is $dV_o = J_o dV$, where $J_o = |\mathbf{J}_o|$ and $\mathbf{J}_o = \partial\mathbf{X}/\partial\mathbf{x}$; while the relation between the volumes in the current and straight configurations is $dv = J_e dV$, where $J_e = |\mathbf{J}_e|$ and $\mathbf{J}_e = \partial\mathbf{r}/\partial\mathbf{x}$. One can show that $\mathbf{J} = \partial\mathbf{r}/\partial\mathbf{X} = (\partial\mathbf{r}/\partial\mathbf{x})(\partial\mathbf{x}/\partial\mathbf{X}) = \mathbf{J}_e\mathbf{J}_o^{-1}$. It follows that $dv = JdV_o = |\mathbf{J}_e\mathbf{J}_o^{-1}|J_o dV = J_e dV$ [35,36].

3.2 Absolute Nodal Coordinate Formulation Tetrahedral Element. In this section, the three-dimensional ANCF four-node (FN) tetrahedral element based on an incomplete polynomial representation, proposed by Pappalardo et al. [37] and shown in Fig. 2, is described. For this element, the nodal coordinate vector is $\mathbf{e} = [(\mathbf{e}^1)^T \ (\mathbf{e}^2)^T \ (\mathbf{e}^3)^T \ (\mathbf{e}^4)^T]^T$, defined in terms of the volume nodal gradients. For the node 1, 2, 3 and 4, the nodal coordinate vectors are defined as $\mathbf{e}^1 = [(\mathbf{r}^1)^T \ (\mathbf{r}^1_\eta)^T \ (\mathbf{r}^1_\zeta)^T \ (\mathbf{r}^1_\chi)^T]^T$, $\mathbf{e}^2 = [(\mathbf{r}^2)^T \ (\mathbf{r}^2_\zeta)^T \ (\mathbf{r}^2_\chi)^T \ (\mathbf{r}^2_\xi)^T]^T$, $\mathbf{e}^3 = [(\mathbf{r}^3)^T \ (\mathbf{r}^3_\chi)^T \ (\mathbf{r}^3_\xi)^T \ (\mathbf{r}^3_\eta)^T]^T$, and $\mathbf{e}^4 = [(\mathbf{r}^4)^T \ (\mathbf{r}^4_\xi)^T \ (\mathbf{r}^4_\eta)^T \ (\mathbf{r}^3_\zeta)^T]^T$, where superscript k refers to the node number, $k = 1,2,3,4$, $\mathbf{r}$ is the global position vector of the node, $\mathbf{r}_\xi = \partial\mathbf{r}/\partial\xi$, $\mathbf{r}_\eta = \partial\mathbf{r}/\partial\eta$, $\mathbf{r}_\zeta = \partial\mathbf{r}/\partial\zeta$, and $\mathbf{r}_\chi = \partial\mathbf{r}/\partial\chi$ are the position-gradient vectors obtained by differentiation with respect to the *volume coordinates* ξ, η, ζ, and χ, respectively. The nodal coordinate vectors can also be defined in terms of the Cartesian nodal gradients as $\mathbf{p}^k = [(\mathbf{r}^k)^T \ (\mathbf{r}^k_{X_1})^T \ (\mathbf{r}^k_{X_2})^T \ (\mathbf{r}^k_{X_3})^T]^T$, $k = 1,2,3,4$, where X_1, X_2, and X_3 are the Cartesian coordinates. Cartesian and volume coordinates are related by the linear transformation $\mathbf{e}^k = \mathbf{T}^k\mathbf{p}^k$, where matrix $\mathbf{T}^k$ defines the relationship between the volume and Cartesian parametrizations. The vector of element nodal coordinates expressed in terms of volume nodal gradients can be written as $\mathbf{e} = [(\mathbf{e}^1)^T \ (\mathbf{e}^2)^T \ (\mathbf{e}^3)^T \ (\mathbf{e}^4)^T]^T$, while in terms of Cartesian gradients as $\mathbf{p} = [(\mathbf{p}^1)^T \ (\mathbf{p}^2)^T \ (\mathbf{p}^3)^T \ (\mathbf{p}^4)^T]^T$. One can therefore write the linear transformation $\mathbf{e} = \mathbf{T}\mathbf{p}$, where $\mathbf{T}$ is a 48×48 constant transformation matrix.

The position vector of an arbitrary material point on the ANCF tetrahedral element is written as $\mathbf{r} = \mathbf{S}\mathbf{e}$, where $\mathbf{e}$ is the vector of the nodal coordinates and $\mathbf{S}$ is the shape function matrix, defined as

$$\mathbf{S} = [s_1\mathbf{I} \ \ s_2\mathbf{I} \ \ s_3\mathbf{I} \ \ s_4\mathbf{I} \ \ s_5\mathbf{I} \ \ s_6\mathbf{I} \ \ s_7\mathbf{I} \ \ s_8\mathbf{I} \ \ s_9\mathbf{I} \ \ s_{10}\mathbf{I} \ \ s_{11}\mathbf{I} \ \ s_{12}\mathbf{I} \ \ s_{13}\mathbf{I} \ \ s_{14}\mathbf{I} \ \ s_{15}\mathbf{I} \ \ s_{16}\mathbf{I}] \quad (3)$$

where $\mathbf{I}$ is the 3×3 identity matrix. The ANCF tetrahedral-element assumed displacement field is defined using a cubic

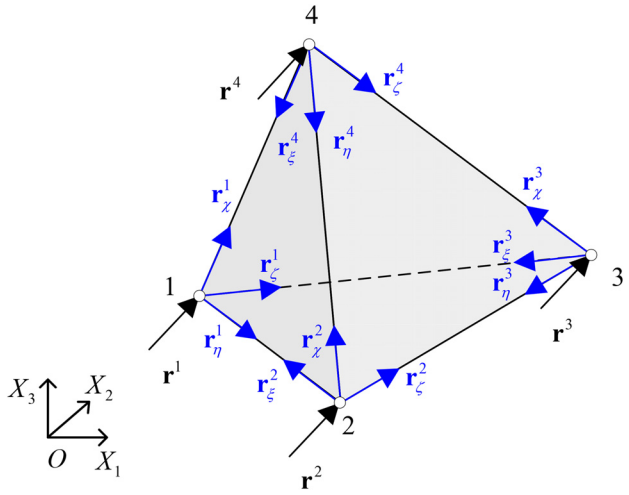

Fig. 2 ANCF tetrahedral element

Bezier tetrahedral patch with 20 basis polynomials and 4 linear vector constraint equations used to eliminate the face-center nodes. The twenty Bezier basis functions are

$$\left.\begin{aligned}
&g_1 = \xi^3, \quad g_2 = \eta^3, \quad g_3 = \zeta^3, \quad g_4 = \chi^3, \quad g_5 = 3\xi^2\eta,\\
&g_6 = 3\xi\eta^2, \quad g_7 = 3\eta^2\zeta, \quad g_8 = 3\eta\zeta^2, \quad g_9 = 3\xi^2\zeta,\\
&g_{10} = 3\xi\zeta^2, \quad g_{11} = 3\xi^2\chi, \quad g_{12} = 3\xi\chi^2, \quad g_{13} = 3\eta^2\chi,\\
&g_{14} = 3\eta\chi^2, \quad g_{15} = 3\zeta^2\chi, \quad g_{16} = 3\zeta\chi^2, \quad g_{17} = 6\xi\eta\zeta,\\
&g_{18} = 6\xi\eta\chi, \quad g_{19} = 6\eta\zeta\chi, \quad g_{20} = 6\xi\zeta\chi
\end{aligned}\right\} \quad (4)$$

By imposing a set of linear constraint equations between the center nodes on the tetrahedral faces and material points on the tetrahedral sides, the displacement field of the ANCF tetrahedral element can be defined using 16 polynomials. In this case, the shape functions of the ANCF tetrahedral element can be defined as

$$\left.\begin{aligned}
&s_1 = \xi\big(\xi^2 + 3\xi(\eta+\zeta+\chi) + 2(\eta\zeta + \chi(\eta+\zeta))\big),\\
&s_2 = \frac{1}{3}\xi\eta(3\xi - \zeta - \chi), \quad s_3 = \frac{1}{3}\xi\zeta(3\xi - \chi - \eta),\\
&s_4 = \frac{1}{3}\xi\chi(3\xi - \eta - \zeta),\\
&s_5 = \eta\big(\eta^2 + 3\eta(\zeta+\chi+\xi) + 2(\zeta\chi + \xi(\zeta+\chi))\big),\\
&s_6 = \frac{1}{3}\eta\zeta(3\eta - \chi - \xi), \quad s_7 = \frac{1}{3}\eta\chi(3\eta - \xi - \zeta),\\
&s_8 = \frac{1}{3}\eta\xi(3\eta - \zeta - \chi),\\
&s_9 = \zeta\big(\zeta^2 + 3\zeta(\chi+\xi+\eta) + 2(\chi\xi + \eta(\chi+\xi))\big),\\
&s_{10} = \frac{1}{3}\zeta\chi(3\zeta - \xi - \eta), \quad s_{11} = \frac{1}{3}\zeta\xi(3\zeta - \eta - \chi),\\
&s_{12} = \frac{1}{3}\zeta\eta(3\zeta - \chi - \xi),\\
&s_{13} = \chi\big(\chi^2 + 3\chi(\xi+\eta+\zeta) + 2(\xi\eta + \zeta(\xi+\eta))\big),\\
&s_{14} = \frac{1}{3}\chi\xi(3\chi - \eta - \zeta), \quad s_{15} = \frac{1}{3}\chi\eta(3\chi - \zeta - \xi),\\
&s_{16} = \frac{1}{3}\chi\zeta(3\chi - \xi - \eta)
\end{aligned}\right\} \quad (5)$$

The detailed steps of the formulation of this ANCF element can be found in the literature [37].

4 Curvature Continuity Conditions

When two cubic ANCF solid elements are connected, the interface surfaces of the two elements are identical as previously discussed in this paper. This is not the case with the ANCF tetrahedral elements because the number of nodal connectivity conditions is not enough to ensure conformal interface surfaces. The curvature continuity conditions can be applied at the nodal points of the ANCF tetrahedral elements in order to achieve a higher degree of smoothness desirable for fluid applications. The ANCF tetrahedral element ensures only the continuity of the displacement gradients at the nodal points. In the work of Wei et al. [28] and Ma et al. [38], a higher degree of continuity across the element interface is achieved by applying curvature constraint equations expressed in terms of the solid element coordinates. In this section, general curvature-continuity conditions are defined using the *structure coordinates*, instead of the element coordinates. The use of the structure coordinates allows developing general conditions applicable to both reference-configuration straight and curved geometries and to meshes with elements that have different orientations [39].

In order to define the general curvature-continuity equations in terms of the structure coordinates, the straight-element and structure coordinates are defined as $\mathbf{x} = [x_1 \;\; x_2 \;\; x_3]^T$, and $\mathbf{X} = [X_1 \;\; X_2 \;\; X_3]^T$, respectively. The structure coordinates can be selected, without any loss of generality, to coincide with the curved-reference coordinates in the stress-free configuration. The matrices of position-vector gradients defined with respect to the element and structure coordinates are defined as $\mathbf{J}_e = [\mathbf{r}_{x_1} \;\; \mathbf{r}_{x_2} \;\; \mathbf{r}_{x_3}]$, $\mathbf{J} = [\mathbf{r}_{X_1} \;\; \mathbf{r}_{X_2} \;\; \mathbf{r}_{X_3}]$, respectively. It follows that $\mathbf{J} = \mathbf{J}_e\mathbf{J}_o^{-1}$, where $\mathbf{J}_o = \mathbf{S}\mathbf{e}_o$ is the matrix of the position-vector gradients that accounts for the stress-free reference configuration. Consequently, one can write curvature-continuity conditions defined using the structure coordinates as $(\mathbf{J})_{X_j} = (\mathbf{J}_e\mathbf{J}_o^{-1})_{X_j} = [\mathbf{r}_{X_1X_j} \;\; \mathbf{r}_{X_2X_j} \;\; \mathbf{r}_{X_3X_j}]$, $j = 1,2,3$. The general expression for the curvatures using the structure coordinates is defined as [39]

$$(\mathbf{J})_{X_j} = \begin{bmatrix} \mathbf{r}_{X_1X_j} & \mathbf{r}_{X_2X_j} & \mathbf{r}_{X_3X_j} \end{bmatrix} = \sum_{k=1}^{3} \left(\mathbf{J}_e\mathbf{J}_o^{-1}\right)_{x_k} \frac{\partial x_k}{\partial X_j}$$
$$= \sum_{k=1}^{3} \left((\mathbf{J}_e)_{x_k}\mathbf{J}_o^{-1} + \mathbf{J}_e\left(\mathbf{J}_o^{-1}\right)_{x_k} \right) \alpha_{kj} \tag{6}$$

where, $(\mathbf{J}_e)_{x_k} = [\mathbf{r}_{x_1x_k} \;\; \mathbf{r}_{x_2x_k} \;\; \mathbf{r}_{x_3x_k}]$, $(\mathbf{J}_o^{-1})_{x_k} = -\mathbf{J}_o^{-1}(\mathbf{J}_o)_{x_k}\mathbf{J}_o^{-1}$, $k = 1,2,3$, and $\alpha_{kj} = \partial x_k/\partial X_j$, $j,k = 1,2,3$. For simplicity, the curvature vectors $\mathbf{r}_{X_iX_j} = \partial^2\mathbf{r}/\partial X_i\partial X_j$, $i,j = 1,2,3$ is written as

$$\mathbf{r}_{X_iX_j} = \sum_{k=1}^{3} \left((\mathbf{J}_e)_{x_k}\mathbf{J}_o^{-1} + \mathbf{J}_e\left(\mathbf{J}_o^{-1}\right)_{x_k} \right) \frac{\partial x_k}{\partial X_j}$$
$$= \sum_{k=1}^{3} \left((\mathbf{J}_e)_{x_k}\mathbf{C}_{Ji} + \mathbf{J}_e\mathbf{C}_{Jxi} \right) \alpha_{kj}$$
$$= \sum_{k=1}^{3} (\alpha_{1i}\mathbf{r}_{x_1x_k} + \alpha_{2i}\mathbf{r}_{x_2x_k} + \alpha_{3i}\mathbf{r}_{x_3x_k})\alpha_{kj}$$
$$+ \sum_{k=1}^{3} (\alpha_{x_k1i}\mathbf{r}_{x_1} + \alpha_{x_k2i}\mathbf{r}_{x_2} + \alpha_{x_k3i}\mathbf{r}_{x_3})\alpha_{kj} \tag{7}$$

where, $\mathbf{C}_{Ji}$ is the ith column of $\mathbf{J}_o^{-1}$, and the matrix $\mathbf{J}_o^{-1}$ can be written as

$$\mathbf{J}_o^{-1} = \begin{bmatrix} \partial x_1/\partial X_1 & \partial x_1/\partial X_2 & \partial x_1/\partial X_3 \\ \partial x_2/\partial X_1 & \partial x_2/\partial X_2 & \partial x_2/\partial X_3 \\ \partial x_3/\partial X_1 & \partial x_3/\partial X_2 & \partial x_3/\partial X_3 \end{bmatrix} = \begin{bmatrix} \alpha_{11} & \alpha_{12} & \alpha_{13} \\ \alpha_{21} & \alpha_{22} & \alpha_{23} \\ \alpha_{31} & \alpha_{32} & \alpha_{33} \end{bmatrix} \tag{8}$$

$\alpha_{kl} = \partial x_k/\partial X_l$, $k,l = 1,2,3$, and α_{x_klm}, $l,m = 1,2,3$ is the lm-th element of matrix $(\mathbf{J}_o^{-1})_{x_k}$, which takes the form

$$(\mathbf{J}_o^{-1})_{x_k} = \begin{bmatrix} \alpha_{x_k11} & \alpha_{x_k12} & \alpha_{x_k13} \\ \alpha_{x_k21} & \alpha_{x_k22} & \alpha_{x_k23} \\ \alpha_{x_k31} & \alpha_{x_k32} & \alpha_{x_k33} \end{bmatrix} \tag{9}$$

Using the general curvature expressions of Eq. (6), different curvature vectors can be equated at two arbitrary points on two different elements of the ANCF mesh. For example, in the case of imposing curvature constraints at two points on two different elements i and j, one can write the curvature vector constraint equations as $\mathbf{r}^i_{X_kX_l} = \mathbf{r}^j_{X_mX_n}$, $k,l,m,n = 1,2,3$.

5 Absolute Nodal Coordinate Formulation Fluid Dynamics Model

In this section, the ANCF fluid dynamic formulation used in this investigation is described. The formulations of the viscous forces and the incompressibility conditions as well as the equations of motion of the ANCF fluid model are introduced. A simple constitutive model is used for the fluid since the focus of this investigation is on the tetrahedral element geometry and the discontinuities at the element interface.

5.1 Viscous Forces. The fluid constitutive model can be written in terms of Cauchy stress tensor $\boldsymbol{\sigma}$ as $\boldsymbol{\sigma} = \{-p + \lambda\mathrm{tr}(\mathbf{D})\}\mathbf{I} + 2\mu\mathbf{D}$. In case of an incompressible fluid, the constitutive equation reduces to $\boldsymbol{\sigma} = 2\mu\mathbf{D}$ [40] In general, when using the Lagrangian approach, the virtual work of the fluid stress forces is written in terms of the second Piola-Kirchkoff stress tensor $\boldsymbol{\sigma}_{P2}$ and the Green-Lagrangian strain tensor $\boldsymbol{\varepsilon}$ as

$$\delta W_v = -\int_v \boldsymbol{\sigma} : (\delta\mathbf{J})(\mathbf{J})^{-1} dv = -\int_{V_o} \boldsymbol{\sigma}_{P2} : \delta\boldsymbol{\varepsilon} dV_o \tag{10}$$

where $\boldsymbol{\sigma}_{P2} = J\mathbf{J}^{-1}\boldsymbol{\sigma}(\mathbf{J}^{-1})^T$, $\boldsymbol{\varepsilon} = (\mathbf{J}^T\mathbf{J} - \mathbf{I})/2$, and $\mathbf{J}$ is the matrix of position-vector gradients. The virtual work of the fluid viscous forces can be written as

$$\delta W_v = -\int_{V_o} \boldsymbol{\sigma}_{P2} : \delta\boldsymbol{\varepsilon} dV_o = -\int_{V_o} 2\mu J(\mathbf{C}_r^{-1}\dot{\boldsymbol{\varepsilon}}\mathbf{C}_r^{-1}) : \delta\boldsymbol{\varepsilon} dV_o = \mathbf{Q}_v^T\delta\mathbf{e} \tag{11}$$

where $\mathbf{C}_r = \mathbf{J}^T\mathbf{J}$ is the right Cauchy-Green deformation tensor, and $\mathbf{Q}_v$ is the vector of generalized viscous forces, which can be written, in terms of the ANCF nodal coordinates as

$$\mathbf{Q}_v = -\int_{V_o} 2\mu J\left(\mathbf{C}_r^{-1}\dot{\boldsymbol{\varepsilon}}\mathbf{C}_r^{-1}\right) : \frac{\partial\boldsymbol{\varepsilon}}{\partial\mathbf{e}} dV_o \tag{12}$$

where the domain of integration in this equation is defined in the stress-free curved-reference configuration V_o. The volume relationship defined by the equation $dV_o = J_o dV$ can be used to change the domain of integration to the straight configuration which can be more convenient, particularly in case of complex reference-configuration geometry.

5.2 Incompressibility Condition. For an incompressible material, $dv = JdV_o = dV$, and as a consequence, the determinant of the matrix of position vector gradients $|\mathbf{J}|$ is equal to one. It follows that $\dot{J} = 0$. Using a penalty method, the penalty energy function $U_{ic} = k_{ic}(J-1)^2/2$ and dissipation energy function $U_{td} = c_{td}(\dot{J})^2/2$ can be formulated and used to define the generalized penalty forces associated with the ANCF nodal coordinates as

$$\left.\begin{aligned}\mathbf{Q}_{ic} &= \partial U_{ic}/\partial \mathbf{e} = k_{ic}(J-1)(\partial J/\partial \mathbf{e})\\ \mathbf{Q}_{td} &= \partial U_{td}/\partial \mathbf{e} = c_{td}\dot{J}(\partial \dot{J}/\partial \dot{\mathbf{e}})\end{aligned}\right\} \tag{13}$$

where $\dot{J} = \mathrm{tr}(\mathbf{D})J$, $\partial \dot{J}/\partial \dot{\mathbf{e}} = \partial J/\partial \mathbf{e}$, and k_{ic} and c_{td} are, respectively, the penalty damping and stiffness coefficients. In the three-dimensional analysis, the determinant of the Jacobian matrix of the position vector gradients can be written as [40,41]:

$$J = \mathbf{r}_{X_1} \cdot (\mathbf{r}_{X_2} \times \mathbf{r}_{X_3}) = \mathbf{r}_{X_2} \cdot (\mathbf{r}_{X_3} \times \mathbf{r}_{X_1}) = \mathbf{r}_{X_3} \cdot (\mathbf{r}_{X_1} \times \mathbf{r}_{X_2}) \tag{14}$$

Therefore, $\partial J/\partial \mathbf{e}$, which is equal to $\partial \dot{J}/\partial \dot{\mathbf{e}}$, can be written explicitly by differentiating any of the three expressions of J given in the preceding equation with respect to $\mathbf{e}$ as [21]

$$\begin{aligned}\partial \dot{J}/\partial \dot{\mathbf{e}} &= \partial J/\partial \mathbf{e}\\ &= \mathbf{S}_{X_1}^T(\mathbf{r}_{X_2} \times \mathbf{r}_{X_3}) + \mathbf{S}_{X_2}^T(\mathbf{r}_{X_3} \times \mathbf{r}_{X_1}) + \mathbf{S}_{X_3}^T(\mathbf{r}_{X_1} \times \mathbf{r}_{X_2})\end{aligned} \tag{15}$$

Using Eq. (13), the total vector of generalized penalty forces of the ANCF fluid element can be written as $\mathbf{Q}_p = \mathbf{Q}_{td} + \mathbf{Q}_{ic}$.

5.3 Equations of Motion. The principle of virtual work and the ANCF displacement field are used in this paper to obtain the equations of motion of the fluid as

$$\mathbf{M}\ddot{\mathbf{e}} = \mathbf{Q}_b + \mathbf{Q}_t + \mathbf{Q}_c - \mathbf{Q}_p + \mathbf{Q}_v \tag{16}$$

where $\mathbf{Q}_b$ and $\mathbf{Q}_t$ are the vectors of generalized body and surface traction forces, respectively, $\mathbf{Q}_c$ is the vectors of generalized contact forces developed in the following section, and $\mathbf{M}$ is the constant symmetric mass matrix. The preceding equation is used to solve for the acceleration vector $\ddot{\mathbf{e}}$, which can be integrated to determine the coordinates and velocities.

6 Boundray Conditions

In the simulation models presented in this study, contact with the ground and contact with containers are considered. In both cases, the fluid is subjected to boundary forces that prevent the fluid from penetrating the ground or container walls. The contact forces, which can be developed using a penalty method, depend on the fluid displacement and velocity as well as the container motion. Therefore, the region of the contact boundary surface of the fluid must be determined as the fluid moves. The resulting problem is referred to as *boundary nonlinearity*.

6.1 Fluid/Ground Contact. For the problem of liquid/ground interaction, the position of a potential contact point P on an ANCF fluid element can be written as $\mathbf{r}_P = \mathbf{S}_P\mathbf{e}$, where $\mathbf{S}_P$ is the element shape function matrix evaluated at the contact point P. The global position of the ground reference point can simply be written as $\mathbf{R}^g = [x_1^g \quad x_2^g \quad x_3^g]^T = \mathbf{0}$. The relative position and velocity vectors of the contact point with respect to the ground reference point can be written, respectively, as $\mathbf{u}_P = \mathbf{S}_P\mathbf{e} - \mathbf{R}^g$ and $\dot{\mathbf{u}}_P = \mathbf{S}_P\dot{\mathbf{e}} - \dot{\mathbf{R}}^g$, where $\dot{\mathbf{e}}$ is the vector of nodal velocities of the fluid element. Using these simple equations, the penetration δ_g can be defined as $\delta_g = \mathbf{u}_P \cdot \mathbf{n}^g - x_3^g$, where $\mathbf{u}_P$ is projected along the unit vector $\mathbf{n}^g$ which defines the direction normal to the contact surface. The time-rate of the penetration is approximated as $\dot{\delta}_g = \dot{\mathbf{u}}_P \cdot \mathbf{n}^g$. Using the penetration and its time-rate, the magnitude of the normal and tangential contact forces can be written as $f_n = k_p\delta + C_p|\delta|\dot{\delta}$ and $f_t = \mu_f f_n$, respectively, where k_p, C_p are penalty stiffness and damping coefficients, and μ_f is the friction coefficient between the fluid and the ground. The vector of the penalty force is written as $\mathbf{F}_p = f_n\mathbf{n}^g - f_t\mathbf{t}^g$, where $\mathbf{t}^g = \mathbf{v}_p/|\mathbf{v}_p|$ is a unit vector in the direction of the tangential relative-velocity vector of the contact point $\mathbf{v}_p = \dot{\mathbf{u}}_P - (\dot{\mathbf{u}}_P \cdot \mathbf{n}^g)\mathbf{n}^g$. In general, the expression for the vector of generalized contact forces associated with the ANCF coordinates can be obtained by using the virtual work of the contact forces and is given by $\mathbf{Q}_c = \mathbf{S}_p^T\mathbf{F}_p$, which can be introduced to the right-hand side of Eq. (16).

6.2 Fluid/Container Contact. In this investigation, the fluid container is assumed to have arbitrarily large displacements including finite rotations. For the problem of sloshing in moving containers, the position of a potential contact point P on an ANCF fluid element can still be written as $\mathbf{r}_P = \mathbf{S}_P\mathbf{e}$. If the container is assumed to be rigid, the global position vector of the contact point on the container surface can be written as $\mathbf{r}_P^c = \mathbf{R}^c + \mathbf{A}^c\bar{\mathbf{u}}_P^c$, where superscript c refers to the container, $\mathbf{R}^c$ and $\mathbf{A}^c$ are, respectively, the global position of the container reference point and the orientation of the container coordinate system with respect to the global coordinate system, and $\bar{\mathbf{u}}_P^c$ is the position vector of the potential contact point with respect to the origin of the container coordinate system. It follows that $\dot{\mathbf{r}}_P^c = \dot{\mathbf{R}}^c + \boldsymbol{\omega}^c \times \mathbf{u}_P^c$, where $\boldsymbol{\omega}^c$ is the angular velocity vector of the container, and $\mathbf{u}_P^c = \mathbf{A}^c\bar{\mathbf{u}}_P^c$. Given the container geometry, the unit vector $\mathbf{n}_P^c$ normal to the container surface at point P can be determined and used to evaluate the penetration as $\delta_c = (\mathbf{r}_P - \mathbf{r}_P^c) \cdot \mathbf{n}_P^c$. The time-rate of penetration can be written as $\dot{\delta}_c = (\dot{\mathbf{r}}_P - \dot{\mathbf{r}}_P^c) \cdot \mathbf{n}_P^c + (\mathbf{r}_P - \mathbf{r}_P^c) \cdot \dot{\mathbf{n}}_P^c$. Because $\dot{\mathbf{n}}_P^c$ is orthogonal to $\mathbf{n}_P^c$ and because of the assumption of the smoothness of the container surface, only the component of the time-rate of penetration along the unit normal to the surface is used in the definition of the normal contact force, that is, $\dot{\delta}_c \approx (\dot{\mathbf{r}}_P - \dot{\mathbf{r}}_P^c) \cdot \mathbf{n}_P^c$. Using the penetration and its time-rate and the virtual work of the contact forces, the generalized contact forces associated with the fluid and the container coordinates $\mathbf{Q}_c$ can be defined using a procedure similar to the one used for the ground contact.

7 Numerical Examples

In this section, a verification numerical study is conducted in order to evaluate the performance of ANCF tetrahedral element by comparing its results with the ANCF solid element in the solution of liquid sloshing problems. Both elements have 12 nodal coordinates per node, three position and nine gradient coordinates. The shape functions of the solid element are provided in the literature [28,42]. Three numerical examples are considered in this section. In the first example, the deformation of a liquid column falling on a flat rigid surface under the effect of gravity is considered. In the second benchmark example, the effect of the liquid sloshing in a rectangular container is investigated. A third example is used to demonstrate using the ANCF tetrahedral element in the analysis of liquid sloshing in a railroad vehicle model negotiating a curve. In order to be able to develop such a model, the ANCF liquid sloshing formulation is systematically integrated with an MBS railroad vehicle algorithm. The results presented in this section are obtained using the general-purpose MBS software **SIGMA/SAMS** (**S**ystematic **I**ntegration of **G**eometric **M**odeling and **A**nalysis for the **S**imulation of **A**rticulated **M**echanical **S**ystems).

7.1 Liquid/Ground Interaction. In this section, the deformation of a liquid column on a flat rigid surface under the effect of gravity is examined. The initial dimensions of the liquid column are $a = b = c = 1$ m, as shown in Fig. 3. The liquid considered is water, with mass density $\rho = 1000\mathrm{kg/m^3}$, and dynamic viscosity coefficient $\mu = 0.001\,\mathrm{Pa \cdot s}$. The simulation time is assumed to be 0.5 s. Figures 4 and 5 show the fluid deformed shape obtained using a mesh of $2 \times 2 \times 2$ ANCF solid and $5 \times (2 \times 2 \times 2)$ ANCF tetrahedral elements, respectively. It is observed that, unlike the solid element mesh, the tetrahedral element mesh does not properly capture the fluid large deformation. The ANCF tetrahedral element results obtained in this example are verified using

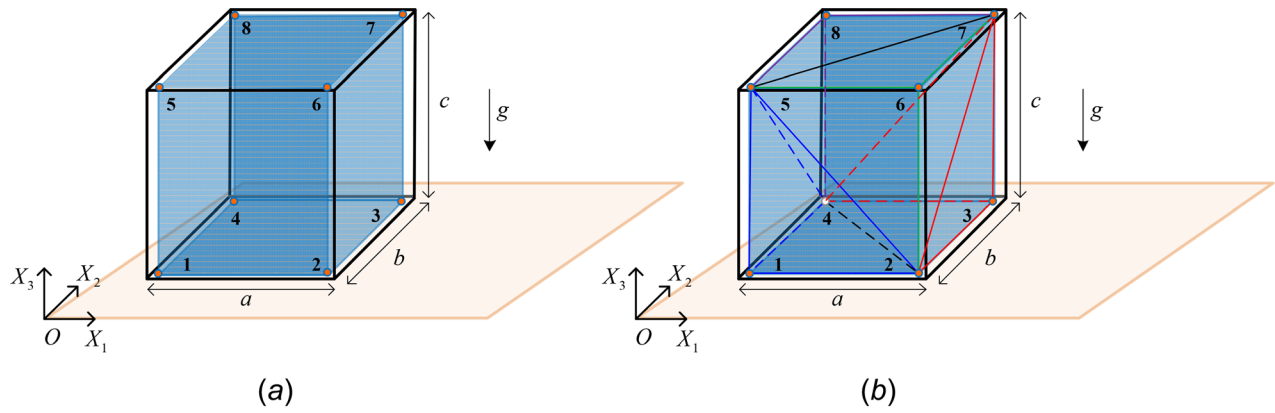

Fig. 3 Fluid/ground surface interaction: (*a*) ANCF solid-element mesh and (*b*) ANCF tetrahedral-element mesh

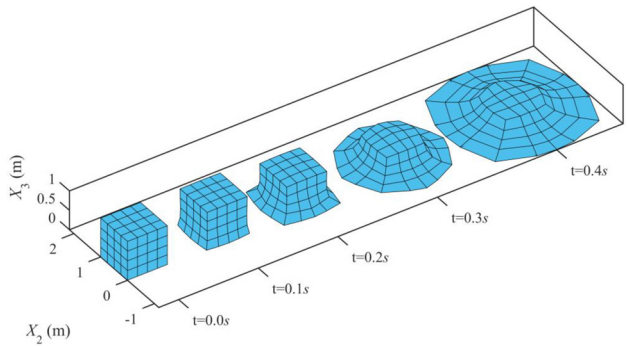

Fig. 4 Liquid/ground interaction simulation (2×2×2 solid elements)

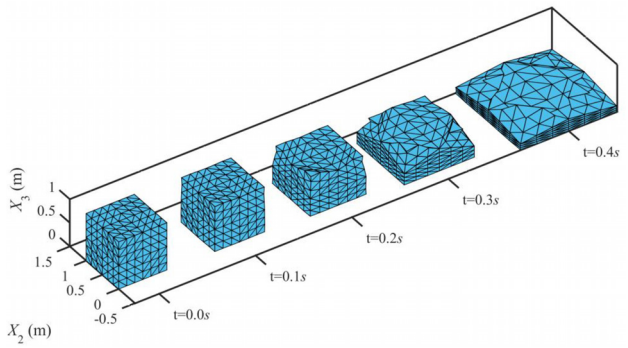

Fig. 5 Liquid/ground interaction simulation (5×(2×2×2) tetrahedral elements)

the four-node Lagrangian tetrahedral element implemented in the commercial software Ls-Dyna. The Ls-Dyna model is assumed to consist of $5 \times (10 \times 10 \times 10)$ elements. The liquid constitutive model is defined using the option "Null material" with Grüneisen equation of state [43]. The algorithm used to define the contact between the liquid and the container boundary is "Boundary SPC" [44]). Figures 6–8 compares the tip displacement at the nodal point $[1 \quad 1 \quad 1]^T$ obtained with the Ls-Dyna and ANCF solutions. The results presented in this figure show that both the vertical and lateral displacements are in relatively good agreement. The deviation shown in the lateral fluid deformation results can be explained by the significant differences in the assumed displacement fields of the two tetrahedral elements. The difference in the results can also be attributed to the discontinuity and jump in the

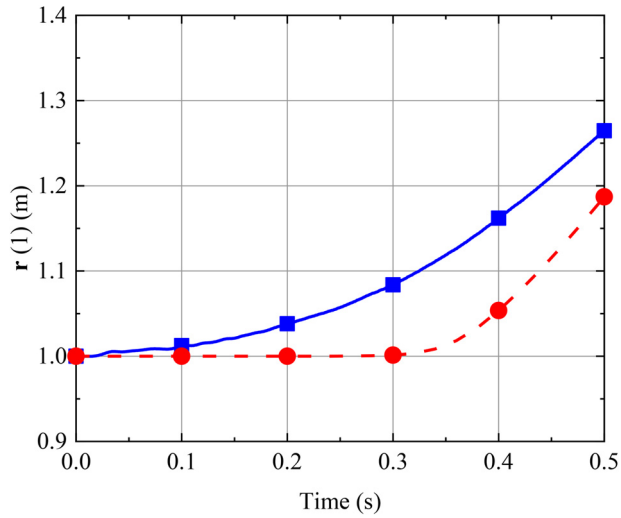

Fig. 6 r(1) tip displacement in the case of liquid/ground interaction (ANCF tetrahedral element, Ls-Dyna tetrahedral element)

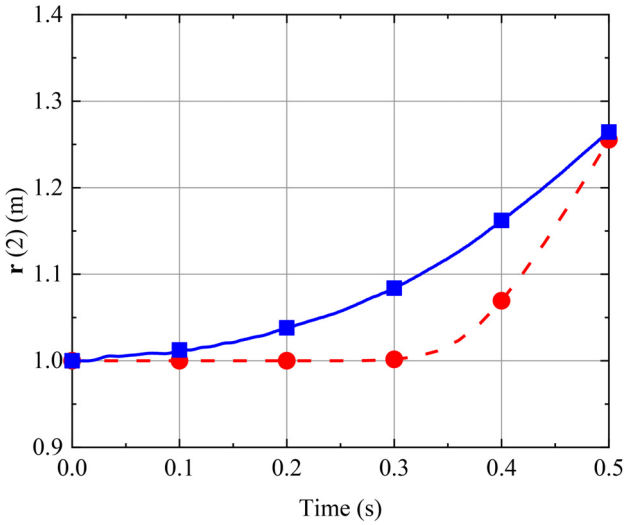

Fig. 7 r(2) tip displacement in the case of liquid/ground interaction (ANCF tetrahedral element, Ls-Dyna tetrahedral element)

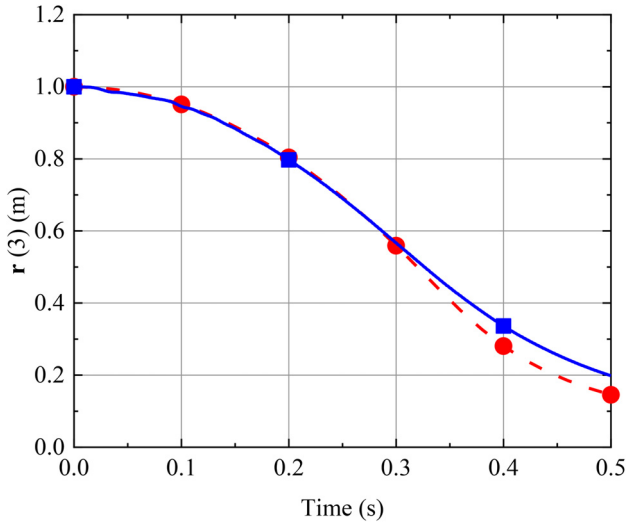

Fig. 8 r(3) tip displacement in the case of liquid/ground interaction (ANCF tetrahedral element, Ls-Dyna tetrahedral element)

viscosity forces at the element interface, which lead to nonsmooth behavior.

7.2 Sloshing in Moving Container. In this example, a rigid container partially filled with water and subjected to a prescribed harmonic motion is considered. The system initial configuration is shown in Fig. 9. The dimensions of the rigid container are $a = b = 1\,\text{m}$, and the liquid depth is $c = 1\,\text{m}$. The container harmonic motion is assumed to be $x_1^c = 0.3\sin(3t)$, and the simulation time is 1.0 s. The fluid model is discretized using ANCF solid and tetrahedral elements. Figures 10 and 11 show the fluid deformation obtained using one ANCF solid element and five ANCF tetrahedral elements. It is observed that the ANCF tetrahedral element mesh leads to a stiffer response as compared to the ANCF solid element mesh. The effect of the gradient vector continuity at the element interface is also studied in this example. Figure 12 shows the time history of the gradient vector coordinates at the central point B on the top surface of the fluid in the case of the five tetrahedral elements mesh. Curvature-continuity conditions are imposed in order to eliminate the gradient discontinuity at the element interface. In the five tetrahedral elements mesh shown in Fig. 9(*b*), the elements at the four corners are $i = E1$ (blue), $j = E2$ (red), $m = E3$ (green), and $n = E4$ (purple). The goal is to enforce the continuity conditions on the top nodes 5 and 7 of

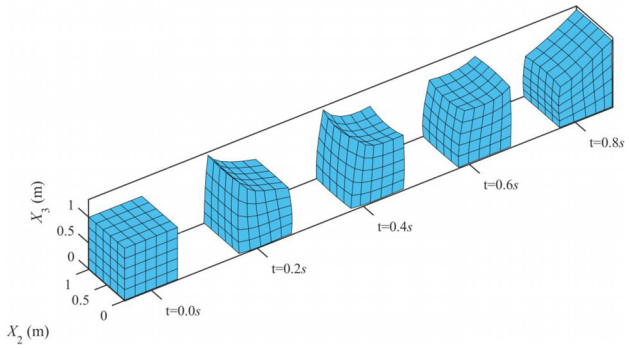

Fig. 10 Liquid sloshing simulation (One solid element)

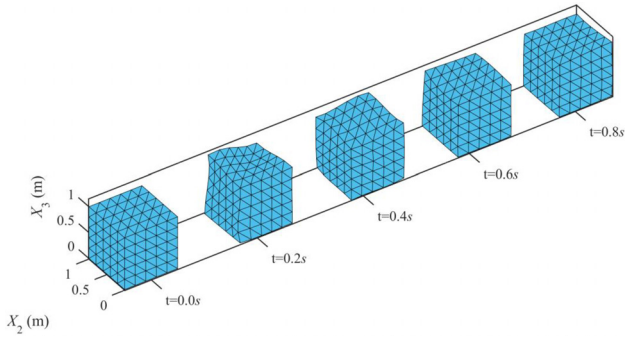

Fig. 11 Liquid sloshing simulation (Five tetrahedral elements)

elements m and n. The resulting curvature constraints are $\mathbf{r}^{m5}_{X_1X_2} = \mathbf{r}^{n5}_{X_1X_2}$, $\mathbf{r}^{m5}_{X_1X_3} = \mathbf{r}^{n5}_{X_1X_3}$, $\mathbf{r}^{m5}_{X_2X_3} = \mathbf{r}^{n5}_{X_2X_3}$ for node 5 and $\mathbf{r}^{m7}_{X_1X_1} = \mathbf{r}^{n7}_{X_1X_1}$, $\mathbf{r}^{m7}_{X_2X_2} = \mathbf{r}^{n7}_{X_2X_2}$, $\mathbf{r}^{m7}_{X_3X_3} = \mathbf{r}^{n7}_{X_3X_3}$ for node 7. These conditions require the formulation of 18 linear algebraic equations, and consequently, the number of degrees-of-freedom of the tetrahedral element mesh is reduced to 78. Figure 13 shows the resulting gradient coordinates at the central point B when the curvature-continuity conditions are applied. While the magnitudes of the position vector gradients are slightly changed, the higher degree of smoothness does not contribute to improving the accuracy of the results when using ANCF tetrahedral elements for this model.

7.3 Sloshing in Railroad Tank. In order to evaluate the tetrahedral element performance in more general motion scenarios, the liquid sloshing formulation based on the ANCF tetrahedral element is systematically integrated with a complex MBS railroad

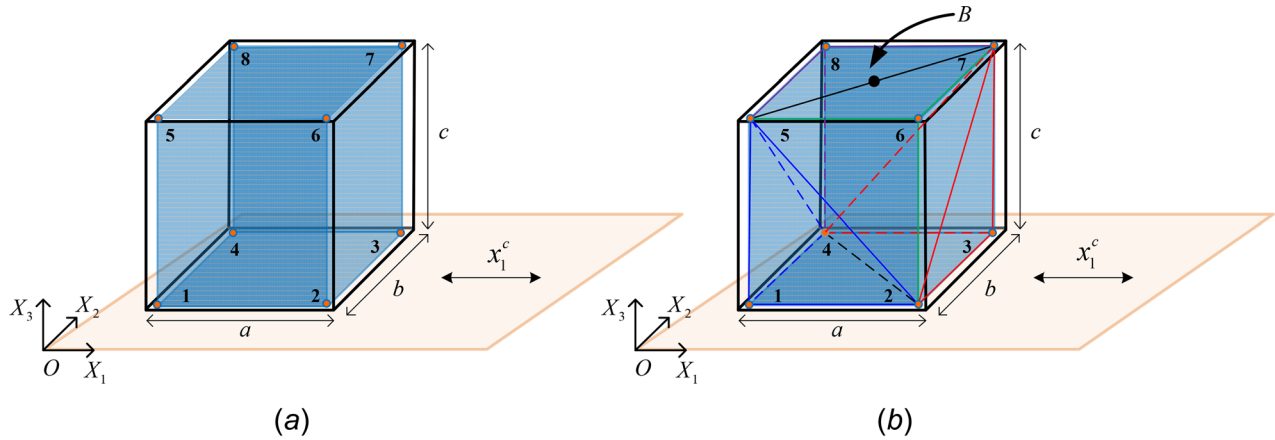

Fig. 9 Liquid sloshing example: (*a*) ANCF solid-element mesh and (*b*) ANCF tetrahedral-element mesh

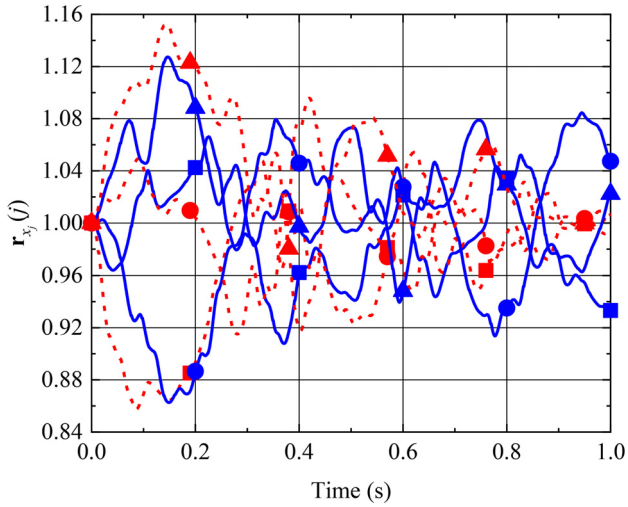

Fig. 12 Gradient coordinates at point *B* predicted using ANCF tetrahedral element in the case of liquid sloshing without curvature constraints ($r_{x_1}(1)$, $r_{x_2}(2)$, $r_{x_3}(3)$), (element 3, element 4)

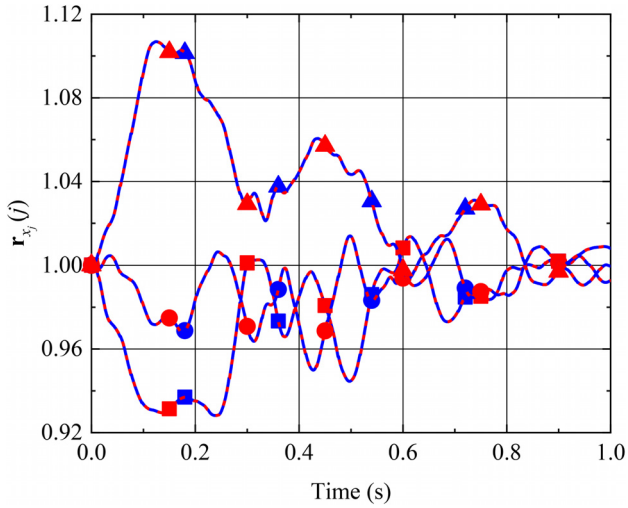

Fig. 13 Gradient coordinates at point *B* predicted using ANCF tetrahedral element in the case of liquid sloshing with curvature constraints ($r_{x_1}(1)$, $r_{x_2}(2)$, $r_{x_3}(3)$), (element 3, element 4)

vehicle model. The detailed MBS railroad vehicle model was previously used by Shi et al. [31] and Grossi and Shabana [33]. This model is a one-car railroad vehicle equipped with a cylindrical tank with half-ellipsoid ends, as shown in Fig. 14. The rail car consists of two bogies, two stub sills, and one tank; each bogie includes two wheelsets, two equalizers, one frame, and one bolster. The one-tank rigid railroad vehicle model has 73 degrees-of-freedom. The dimensions and inertia properties of each car are the same as those presented in the literature [45]. The wheel/rail contact formulation and algorithm used in this paper can be found in the literature [46,47].

The liquid sloshing motion resulting from the railroad vehicle negotiating a curved track is studied in order to investigate the effect on the vehicle dynamics and centrifugal forces. The tank is assumed partially filled with water in order to produce significant sloshing. The balance vehicle speed is defined in case of rigid body dynamics as $V = \sqrt{gRh/G}$ [47], where g is gravity constant,

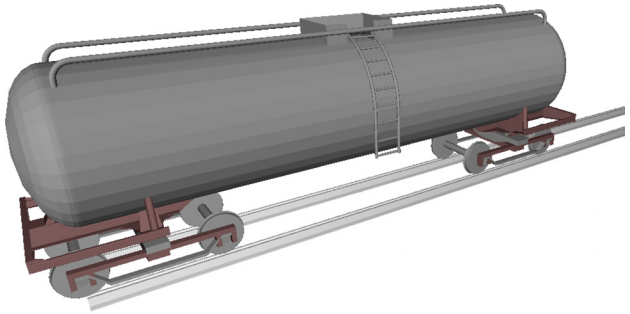

Fig. 14 Railroad vehicle model

R is the radius of curvature of the curve, h is the super-elevation, and G is the track gauge. The track has a radius of curvature $R = 582\,\text{m}$, a track gauge $G = 1.44\,\text{m}$; and therefore, the vehicle balance speed is close to 60km/h. The geometry of the curved track is defined in Table 1. The railroad vehicle forward velocity, assumed 60km/h, is defined using a trajectory coordinate constraint along the track centerline.

When the ANCF liquid sloshing approach is used, the fluid centrifugal force can be calculated as $F_c = \int_{V_o} \rho \ddot{\mathbf{r}} \cdot \mathbf{n} dV_o$, where $\ddot{\mathbf{r}}$ is the absolute acceleration vector of an arbitrary fluid point, and $\mathbf{n}$ is the outward unit normal to the curve [32]. In this study, the centrifugal force is approximated as $F_c = (m_f \ddot{\mathbf{r}}_c) \cdot \mathbf{n}$, where m_f is the total mass of the ANCF fluid mesh, $\ddot{\mathbf{r}}_c$ is the absolute acceleration vector of the body center of mass. The position of the fluid center of mass can be calculated using the equation $\mathbf{r}_c = (\int_{V_o} \rho \mathbf{r} dV_o)/m_f$. The tetrahedral and solid element meshes used in this example consist of 160 and 32 elements, respectively. Figure 15 shows comparison of the centrifugal force calculated using solid and tetrahedral element meshes. Figure 16 compares the mass-center X_2-displacement results predicted using the solid and tetrahedral element meshes. Figures 17 and 18 show the free surface deformation at time $t = 15\,\text{s}$ obtained using solid and tetrahedral elements. It is shown that a nonsmooth deformation can be found at the fluid free surface when the ANCF tetrahedral elements are used. The nonsmooth behavior is attributed to the gradient discontinuity problem at the tetrahedral element interface.

8 Conclusions

In this numerical verification study, the performance of the ANCF tetrahedral element is evaluated when used in the analysis of liquid motion problems. Because the Navier–Stokes viscosity forces are written in terms of the time-rate of the position gradients, continuity of such gradients in the case of laminar flow is necessary in order to obtain accurate solutions. In the FE numerical solution of fluid dynamics problems, the viscosity forces are evaluated at the integration points; some of which are not nodal points. The continuity of the position vector gradients at the nodal points does not ensure the continuity of these gradients at the element interface. For a cubic Bezier surface, 48 connectivity conditions are required in order to ensure that two surfaces on two different elements are identical. While this is the case when using the ANCF solid elements which have four nodes for each of the element six surfaces, it is not case with the ANCF tetrahedral element which has three nodes for each surface. In this paper the performance of the ANCF tetrahedral element in solving sloshing problem was investigated and compared with the performance of the ANCF solid element. The results obtained in this study show that, in general, the free surface of the fluid model can be accurately captured using ANCF solid elements, while the tetrahedral element mesh leads to a stiffer response. This conclusion is also confirmed by the sloshing results obtained using a railroad vehicle negotiating a curved track. The stiff liquid sloshing response

Table 1 Curved track geometry

Segment points No.	Distance (ft)	Curvature (Deg.)	Super-elevation (in)	Grade (%)	Right rail cant angle (rad)	Left rail cant angle (rad)
A	0	0	0	0	0.025	−0.025
B	100	0	0	0	0.025	−0.025
C	300	3	3	0	0.025	−0.025
D	600	3	3	0	0.025	−0.025
E	800	0	0	0	0.025	−0.025
F	1000	0	0	0	0.025	−0.025
G	1200	−3	−3	0	0.025	−0.025
H	1500	−3	−3	0	0.025	−0.025
I	1700	0	0	0	0.025	−0.025
J	2800	0	0	0	0.025	−0.025

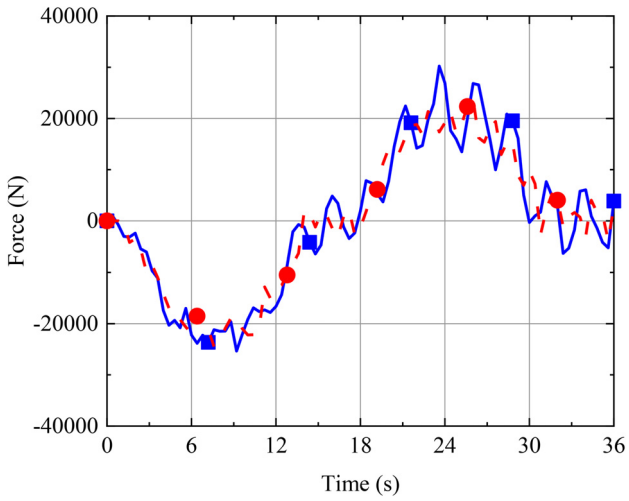

Fig. 15 Centrifugal force comparison (ANCF solid element, ANCF tetrahedral element)

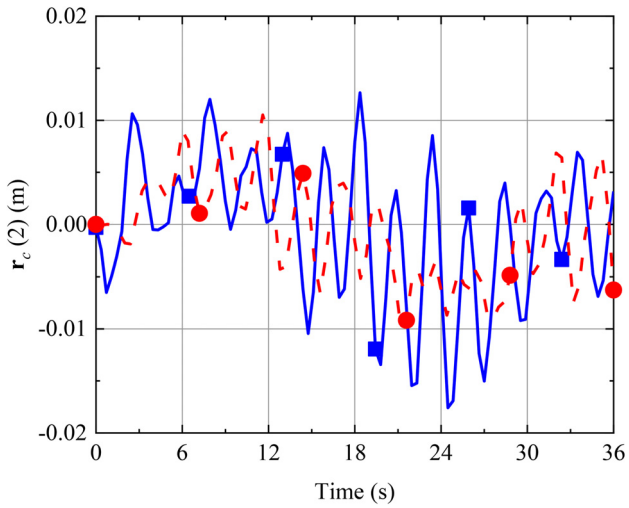

Fig. 16 Mass-center X_2-displacement of the rail tank (ANCF solid element, ANCF tetrahedral element)

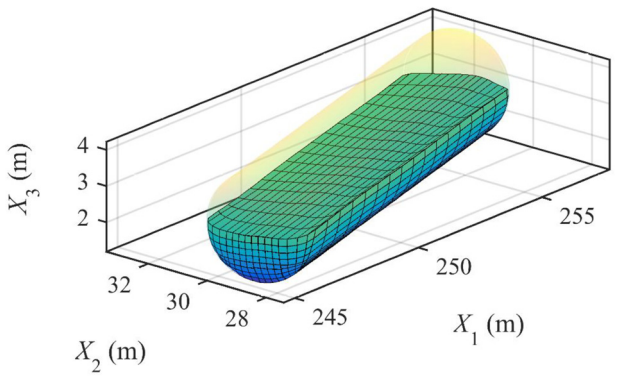

Fig. 17 Curve negotiation simulation at $t = 15$ s (ANCF solid-element mesh)

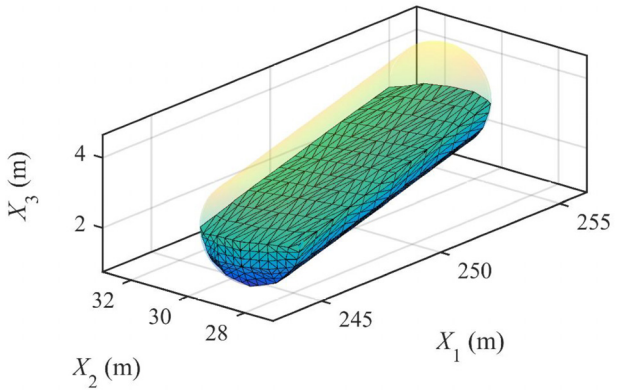

Fig. 18 Curve negotiation simulation at $t = 15$ s (ANCF tetrahedral-element mesh)

predicted using ANCF tetrahedral elements can be attributed to the discontinuity at the element interface which lead to nonsmooth behavior and jump in the viscosity forces at the element interface. The results also show that a higher degree of smoothness at the element interface can be achieved by applying *curvature-continuity* conditions. Nonetheless, such smoothness does not contribute to improving the accuracy of the results when using ANCF tetrahedral elements.

Funding Data

- National Science Foundation (Projects No. 1632302; Funder ID: 10.13039/100000001).

References

[1] Ibrahim, R. A., 2005, *Liquid Sloshing Dynamics: Theory and Applications*, Cambridge University Press, Cambridge, UK.

[2] Ibrahim, R. A., 2015, "Recent Advances in Physics of Fluid Parametric Sloshing and Related Problems," ASME J. Fluids Eng., **137**, p. 090801.

[3] Ibrahim, R. A., Pilipchuk, V. N., and Ikeda, T., 2001, "Recent Advances in Liquid Sloshing Dynamics," ASME Appl. Mech. Rev., **54**(2), pp. 133–199.

[4] Dodge, F. T., and Kana, D. D., 1966, "Moment of Inertia and Damping of Liquid in Baffled Cylindrical Tanks," J. Spacecr. Rockets., **3**(1), pp. 153–155.
[5] Kana, D. D., 1987, "A Model for Nonlinear Rotary Slosh in Propellant Tanks," J. Spacecr. Rockets., **24**(2), pp. 169–177.
[6] Kana, D. D., 1989, "Validated Spherical Pendulum Model for Rotary Liquid Slosh," J. Spacecr. Rockets., **26**(3), pp. 188–195.
[7] Pinson, L. D., 1964, "Longitudinal Spring Constants for Liquid Propellant Tanks with Ellipsoidal Tanks," NASA, Washington, DC, Report No. NASA TN D-2220.
[8] Sumner, I. E., 1965, "Experimentally Determined Pendulum Analogy of Liquid Sloshing in Spherical and Oblate-Spherical Tanks," NASA, Washington, DC, Report No. NASA TN D-2737.
[9] Ranganathan, R., Rakheja, S., and Sankar, S., 1989, "Steady Turning Stability of Partially Filled Tank Vehicles With Arbitrary Tank Geometry," ASME J. Dyn. Syst. Meas. Control, **111**(3), pp. 481–489.
[10] Aliabadi, S., Johnson, A., and Abedi, J., 2003, "Comparison of Finite Element and Pendulum Models for Simulation of Sloshing," Comput. Fluids, **32**(4), pp. 535–545.
[11] Versteeg, H. K., and Malalasekera, W., 2007, *An Introduction to Computational Fluid Dynamics: The Finite Volume Method*, 2nd ed., Pearson/Prentice Hall, Upper Saddle River, NJ.
[12] Reddy, J. N., and Gartling, D. K., 2001, *The Finite Element Method in Heat Transfer and Fluid Dynamics*, 2nd ed., CRC Press, Boca Raton, FL.
[13] Zienkiewicz, O. C., Nithiarasu, P., and Taylor, R. L., 2005, *The Finite Element Method for Fluid Dynamics*, 6th ed., Elsevier Butterworth-Heinemann, Amsterdam.
[14] Anderson, J. D., 1995, *Computational Fluid Dynamics: The Basics With Applications*, McGraw-Hill, New York.
[15] Zikanov, O., 2010, *Essential Computational Fluid Dynamics*, Wiley, Hoboken, NJ.
[16] Gingold, R. A., and Monaghan, J. J., 1977, "Smoothed Particle Hydrodynamics: Theory and Application to Non-Spherical Stars," Mon. Not. R. Astrono. Soc., **181**(3), pp. 375–389.
[17] Liu, M. B., and Liu, G. R., 2010, "Smoothed Particle Hydrodynamics (SPH): an Overview and Recent Developments," Arch. Comput. Methods Eng., **17**(1), pp. 25–76.
[18] Monaghan, J. J., 1988, "An Introduction to SPH," Comput. Phys. Commun., **48**(1), pp. 89–96.
[19] Monaghan, J. J., 1992, "Smoothed Particle Hydrodynamics," Annu. Rev. Astron. Astrophys., **30**(1), pp. 543–574.
[20] Monaghan, J. J., 1994, "Simulating Free Surface Flows With SPH," J. Comput. Phys., **110**(2), pp. 399–406.
[21] Wang, L., Octavio, J. R. J., Wei, C., and Shabana, A. A., 2015, "Low Order Continuum-Based Liquid Sloshing Formulation for Vehicle System Dynamics," ASME J. Comput. Nonlinear Dyn., **10**, p. 021022.
[22] Hirt, C. W., Amsden, A. A., and Cook, J. L., 1997, "An Arbitrary Lagrangian–Eulerian Computing Method for All Flow Speeds," J. Comput. Phys., **135**(2), pp. 203–216.
[23] Hughes, T. J., Liu, W. K., and Zimmermann, T. K., 1981, "Lagrangian-Eulerian Finite Element Formulation for Incompressible Viscous Flows," Comput. Methods Appl. Mech. Eng., **29**(3), pp. 329–349.
[24] Navti, S. E., Ravindran, K., Taylor, C., and Lewis, R. W., 1997, "Finite Element Modelling of Surface Tension Effects Using a Lagrangian-Eulerian Kinematic Description," Comput. Methods Appl. Mech. Eng., **147**(1–2), pp. 41–60.
[25] Onate, E., and Garcia, J., 2001, "A Finite Element Method for Fluid–Structure Interaction With Surface Waves Using a Finite Calculus Formulation," Comput. Methods Appl. Mech. Eng., **191**(6–7), pp. 635–660.
[26] Soulaimani, A., and Saad, Y., 1998, "An Arbitrary Lagrangian-Eulerian Finite Element Method for Solving Three-Dimensional Free Surface Flows," Comput. Methods Appl. Mech. Eng., **162**(1–4), pp. 79–106.
[27] Belytschko, T., Liu, W. K., Moran, B., and Elkhodary, K., 2013, *Nonlinear Finite Elements for Continua and Structures*, Wiley, New York.
[28] Wei, C., Wang, L., and Shabana, A. A., 2015, "A Total Lagrangian ANCF Liquid Sloshing Approach for Multibody System Applications," ASME J. Comput. Nonlinear Dyn., **10**(5), p. 051014.
[29] Grossi, E., and Shabana, A. A., 2017, "Validation of a Total Lagrangian ANCF Solution Procedure for Fluid–Structure Interaction Problems," ASME J. Verif. Valid. Uncertainty Quantif., **2**(4), p. 041001.
[30] Atif, M., Chi, S. W., Grossi, E., and Shabana, A. A., 2019, "Evaluation of Breaking Wave Effects in Liquid Sloshing Problems: ANCF/SPH Comparative Study," Nonlinear Dyn., **97**(1), pp. 45–62.
[31] Shi, H., Wang, L., Nicolsen, B., and Shabana, A. A., 2017, "Integration of Geometry and Analysis for the Study of Liquid Sloshing in Railroad Vehicle Dynamics," Proc. Inst. Mech. Eng., Part K: J. Multi-Body Dyn., **231**(4), pp. 608–629.
[32] Nicolsen, B., Wang, L., and Shabana, A., 2017, "Nonlinear Finite Element Analysis of Liquid Sloshing in Complex Vehicle Motion Scenarios," J. Sound Vib., **405**, pp. 208–233.
[33] Grossi, E., and Shabana, A. A., 2018, "ANCF Analysis of the Crude Oil Sloshing in Railroad Vehicle Systems," J. Sound Vib., **433**, pp. 493–516.
[34] Gonzalez, J. A., Lee, Y. S., and Park, K. C., 2017, "Stabilized Mixed Displacement–Pressure Finite Element Formulation for Linear Hydrodynamic Problems With Free Surfaces," Comput. Methods Appl. Mech. Eng., **319**, pp. 314–337.
[35] Bonet, J., and Wood, R. D., 1997, *Nonlinear Continuum Mechanics for Finite Element Analysis*, Cambridge University Press, Cambridge, UK.
[36] Shabana, A. A., 2018, *Computational Continuum Mechanics*, 3rd ed., Cambridge University Press, Cambridge, UK
[37] Pappalardo, C. M., Wang, T., and Shabana, A. A., 2017, "Development of ANCF Tetrahedral Finite Elements for the Nonlinear Dynamics of Flexible Structures," Nonlinear Dyn., **89**(4), pp. 2905–2932.
[38] Ma, C., Wang, R., Wei, C., and Zhao, Y., 2016, "A New Absolute Nodal Coordinate Formulation of Solid Element With Continuity Condition and Viscosity Model," Int. J. Simul.: Syst., Sci. Technol., **17**(21), pp. 10.1–10.6.
[39] Shabana, A. A., and Zhang, D. Y., 2020, "ANCF Curvature Continuity: Application to Soft and Fluid Materials," Nonlinear Dyn., **100**(2), pp. 1497–1517.
[40] Spencer, A. J. M., 1980, *Continuum Mechanics*, Longman, London, UK.
[41] Ogden, R. W., 1984, *Non-Linear Elastic Deformations*, Dovers Publications, Mineola, NY.
[42] Olshevskiy, A., Dmitrochenko, O., and Kim, C. W., 2014, "Three-Dimensional Solid Brick Element Using Slopes in the Absolute Nodal Coordinate Formulation," ASME J. Comput. Nonlinear Dyn., **9**(2), pp. 1–10.
[43] Grüneisen, E., 1912, "Theorie Des Festen Zustandes Einatomiger Elemente," Ann. Phys., **344**(12), pp. 257–306.
[44] LS-DYNA, 2018, "LS-DYNA keyword user's manual," LSTC, Livermore, CA.
[45] Shabana, A. A., Tobaa, M., Sugiyama, H., and Zaazaa, K., 2005, "On the Computer Formulations of the Wheel/Rail Contact Problem," Nonlinear Dyn., **40**(2), pp. 169–193.
[46] Berzeri, M., Sany, J. R., and Shabana, A. A., 2000, "Curved Track Modeling Using the Absolute Nodal Coordinate Formulation," University of Illinois, Chicago, IL, Report No. MBS00-4-UIC.
[47] Shabana, A. A., Zaazaa, K. E., and Sugiyama, H., 2008, *Railroad Vehicle Dynamics: A Computational Approach*, Taylor & Francis/CRC, Boca Raton, FL.